Soft Body Impact on Composites : Delamination experiments and Advanced Numerical Modelling

Jagan Selvaraj[a], Luiz F. Kawashita[a], Mehdi Yasaee[b], Gordon Kalwak[c,d], Stephen R. Hallett[a]

[a]*Bristol Composite Institute (ACCIS), University of Bristol, Queen's Building, University Walk, Bristol BS8 1TR, UK*
[b]*School of Aerospace, Transport and Manufacturing, Cranfield University, MK43 0AL, UK*
[c]*Department of Engineering Science, University of Oxford, Oxford, UK*
[d]*Rolls-Royce plc, Derby, UK*

Abstract

Cohesive interface elements have become commonly used for modelling composites delamination. However, a limitation of this technique is the fine mesh size required. Here, a novel cohesive element formulation is proposed and demonstrated for modelling the numerical cohesive zone with equal fidelity but fewer elements in comparison to a linear cohesive element formulation. The newly proposed formulation has additional degrees of freedom in the form of nodal rotations which when combined with the use of multiple integration points per cohesive element, allows for delamination propagation to be modelled with increased stability. This element formulation is introduced with an adaptive modelling method, termed Adaptive Mesh Segmentation (AMS). To demonstrate its effectiveness under impact loading the new model is applied to a soft body beam bending test. This test, containing a delamination precrack, uses inertial constraints and results in a dynamic stress state when impacted by a gelatin cylinder.

Keywords: Impact behaviour, Delamination, Finite element analysis (FEA), Cohesive element formulation

1. Introduction

The superior specific strength and stiffness provided by laminated composite structures allows for the design of energy efficient aerospace components. During the service life, they are subjected to various loading conditions including low velocity (tool drops during maintenance) and high velocity impact (strike of debris or other foreign objects). High interlaminar stress can be induced by dynamic events such as impact [1, 2], with delamination being one of the most critical failure phenomena [3], usually accompanied by matrix cracking and ultimately fibre failure. Hence, in the design of composite structures, understanding damage and the resulting loss of stiffness is of vital importance. Numerical modelling of such events is generally performed using an energy based approach that can produce mesh independent results. Cohesive zone modelling (CZM) has become the preferred numerical technique to characterise delamination behaviour in composite structures [4, 5, 6, 7]. CZM is characterised by the presence of two constitutive relations: (i) a constitutive relation for stress and strain in the continuum and (ii) a cohesive relation that for traction and separation across a discontinuity.

A limiting requirement to discretise the numerical cohesive zone with multiple integration points results in a highly refined mesh when modelled with linear elements. Different strategies have been adopted in the existing literature to allow for computations with coarser meshes.

Artificial interface strength reduction has been used along with linear elements to increase the length of numerical cohesive zone when a coarser mesh is used [6]. Although this improves the discretisation requirement, the accuracy of the method is limited and demonstrated with benchmark cases by Harper and Hallett [8].

In addition to CZM, as used in the current work, delamination modelling can also

be performed using the Virtual crack closure Technique (VCCT) [9] and Continuum Damage Mechanics (CDM) [10]. VCCT assumes that the energy released ΔE_1 during the extension of a crack by Δa is identical to the energy required to close to the crack ΔE_2. The crack or delamination progression is further determined by comparing against the critical energy release rate [11]. However, VCCT requires the presence of an existing crack. Unlike CZM and VCCT, CDM does not model discrete cracks. The damage onset is typically calculated using a stress-based criterion; the damage progression is modelled with an energy-regularised criterion. The damage calculated by CDM models degrades the properties of whole element or ply [10] and hence it is not suited for modelling discrete cracks and large crack opening displacements.

Modelling discontinuities by explicitly forming the crack surfaces within an existing mesh are performed using discrete crack models. They are classified, based on the enrichment method used to introduce discontinuities, into two categories, (i) methods that model discontinuities with the enrichment obtained from additional shape functions [12, 13] and (ii) methods that use standard shape functions in order to simplify the implementation in a commercial FE software [14, 15, 16]. However, many of the existing methods use an implicit time integration scheme.

To obtain the structural response following impact, the impact event and the subsequent propagation of waves must be accurately modelled. The impact event causes an instantaneous change in the velocity and a step change in the solution behaviour - an ill-posed problem. It induces high frequency waves in the material and requires a small time step to study that wave. Hence, an explicit time integration scheme is required [17]. In explicit methods, the global time step is calculated based on element time steps; if the above mentioned methods to model discontinuities are used, splitting of elements following the formation of crack surfaces will result in the subsequent reduction of element time steps and hence the global time step. Such a scenario will

be computationally very expensive in the analysis of structural components. Also, mapping of information to the newly created elements can cause numerical oscillations. Hence, a method that models discontinuities without reducing the time step, while allowing coarser meshes, is required, in particular for impact loading.

A novel cohesive element which uses coordinate rotations has been proposed to enhance the mesh size capability over linear elements [18]. The additional rotational degrees of freedom, coordinate rotations, allow for modelling of displacement across the crack surfaces with C^1 continuity, providing improved resolution in the numerical cohesive zone. These additional degrees of freedom present at the location of nodes makes it compatible with existing 8 noded meshes and this results in fewer degrees of freedom than a quadratic cohesive element formulation which requires 20 noded meshes. Furthermore, multiple integration points can be employed within a cohesive element improving the discretisation of numerical cohesive zone length. Since the spacing of integration points is smaller than linear elements at a given mesh size, stable crack propagation is possible even when using coarser mesh sizes. Hence, accurate results can be obtained with rotation enabled cohesive segments and this is described with numerical examples in [18].

In the current work, this novel cohesive element formulation is applied to the challenging case of a soft body impact and shown to perform well in regards to delamination predictions and also computational efficiency.

Adaptive Mesh Segmentation (AMS) [19] based on a 'simplified cohesive segment' [16] may offer a possible solution to maintain a constant global time step and to avoid numerical oscillations. This method enables automatic insertion of cohesive elements, at element boundaries, to maintain a constant time step size following crack initiation. Moreover, a traction vector calculated from the element nodal forces is also included in the AMS method to increase compatibility with the surrounding

stress field and minimise residuals associated with the initiation. Although methods have been suggested in the past to smear the residuals [20], minimisation of such errors in explicit time integration is an integral feature of this method.

Experimental methods such as three point bend tests along with impact loading are commonly used to understand delamination initiation and progression in composite specimens [21, 22]. Following impact, matrix cracks originates around the location of impact and the ends of the beam which is followed by delamination. The effects of boundary conditions are unavoidable. In order to create representative damage events following a soft body impact on aerospace components, the soft body beam bending (SBBB) test was invented [23]. The SBBB test is a modified three point bend test which uses inertial boundary conditions and so avoids unwanted failures at these locations. The impact triggers through thickness shear loading around the site of impact followed by a bending response in the beam, which can change in curvature depending on the initial impact velocity and inertial constraints.

2. Soft Body Beam Bend Test - Experiments

The Soft Body Beam Bend (SBBB) test [23] is a modified three point beam bending test, in which the beam is suspended from above, with low rotational inertia fittings clamped on the beam ends to provide inertial restraint to translational movement whilst avoiding localised stress and unrealistic failure of the specimen The SBBB aims to replicate the dynamic stress state that occurs following impact on an in-service composite component. The objectives of this experimental method are (i) to determine the threshold velocity, which is defined as the velocity at which full delamination is obtained along the length of a specimen, (ii) to determine the effectiveness of through thickness reinforcements [24] and (iii) to provide experimental

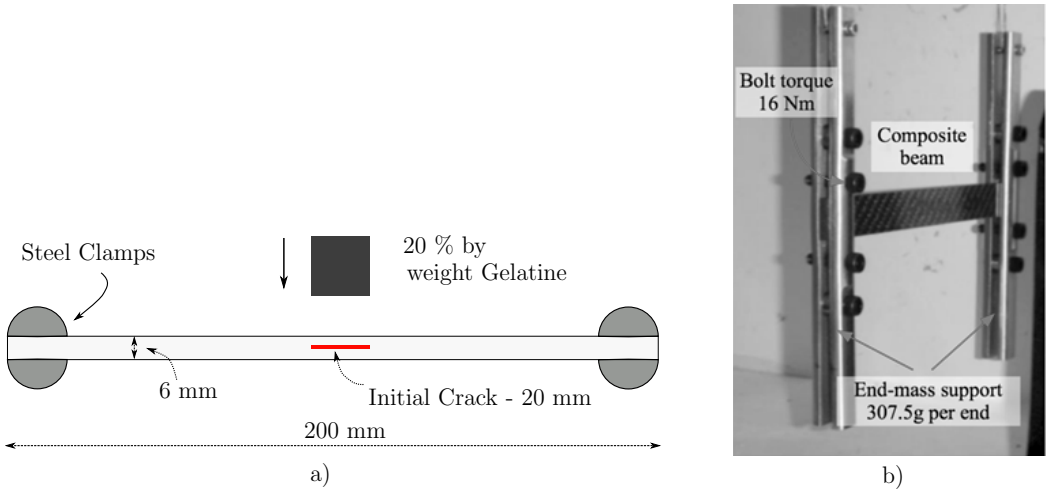

Figure 1: a) Schematics of the SBBB test setup; all specimens have a width of 20 mm. b) Experimental setup.

results with a pre-defined set up that can be replicated in numerical models and analyse the influence of material parameters.

The schematics of the SBBB test and the specimen dimensions are shown in Figure 1. The specimen is fastened to the steel end clamps with a torque of 16 N·m, which are then suspended from long cables. The time period of the system can be varied by adjusting the mass of the clamps, *i.e.* an increase in the mass of the clamps results in the time period of the clamps being higher than the system and the composite specimen. This will force a change in the curvature of the specimen when subjected to impact, changing the resulting concavity of the specimen.

Composite specimens manufactured from carbon fibre epoxy material (IM7/8552) were used in the current work. A symmetric, balanced layup sequence of $((\ 0,\text{-}45,\ 0,\ 45)_{3S})_S$ was used, with a total laminate thickness of 6 mm. A pre-crack of length 20 mm was manufactured into the specimens at their mid-planes, using 5µm thick metal shim material [25]. Under impact loading the delamination growth originates

from the pre-crack tip and grows away from the impact location. Ballistic gelatine (20% by weight) is used for the impactor material. The impactor was cylindrical in shape with length and diameter 20 mm, and a mass of 6.5 g.

3. Modelling Details

3.1. Cohesive Elements with Rotations

In linear cohesive elements with four integration points, a crack can traverse the entire element length in a single time increment when the energy release rate associated with an integration point exceeds the fracture energy. In order to avoid numerical instabilities associated with the rate of crack growth, and to provide sufficient resolution of the numerical cohesive zone bridging forces, an alternative cohesive element formulation is required.

The proposed cohesive element results in a reduction in the area associated with an integration point by allowing the presence of multiple integration points and crack traverses the cohesive element in a finite time.

It should be noted that increasing the number of integration points in a linear cohesive segment does not result in a change in the order of continuity and so the new formulation is augmented with additional degrees of freedom. Full details of the new element formulation are given in [18] and so only the essential features are recounted briefly here.

The non-linear displacement field can be represented by two different configurations: (i) with additional rotational degrees of freedom at the corner nodes or, (ii) by inserting virtual mid-side nodes and calculating their equivalent displacement. The first configuration is used in the calculation of cohesive forces from cohesive tractions while the second is used in the evaluation of this traction vector from the cohesive law,

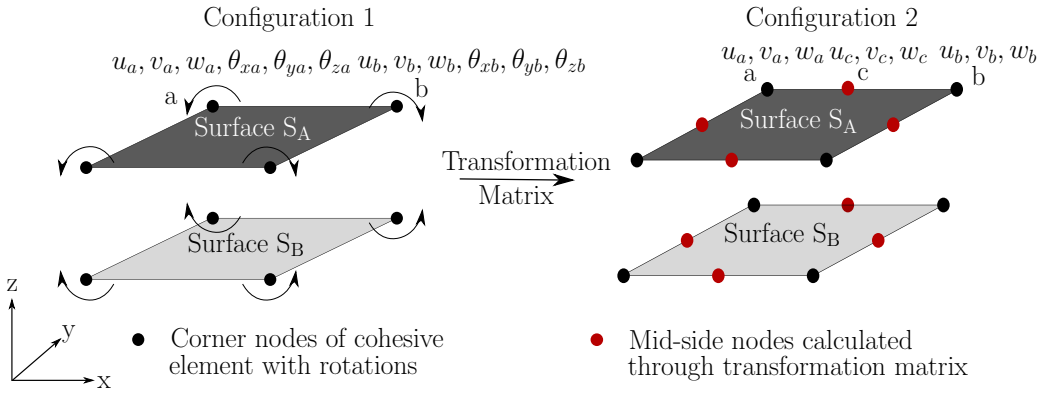

Figure 2: Kinematics in a cohesive segment.

since it is described only using translations. The two configurations are graphically shown in Figure 2. The calculation of equivalent displacement in one of the mid side nodes, c is obtained from the corner nodes a and b by,

$$u_c = \frac{(u_a + u_b)}{2} + \frac{y_b - y_a}{8}(\theta_{zb} - \theta_{za}) + \frac{z_b - z_a}{8}(\theta_{ya} - \theta_{yb}) \tag{1}$$

$$v_c = \frac{(v_a + v_b)}{2} + \frac{z_b - z_a}{8}(\theta_{xb} - \theta_{xa}) + \frac{x_b - x_a}{8}(\theta_{za} - \theta_{zb}) \tag{2}$$

$$w_c = \frac{(w_a + w_b)}{2} + \frac{x_b - x_a}{8}(\theta_{yb} - \theta_{ya}) + \frac{y_b - y_a}{8}(\theta_{xa} - \theta_{xb}) \tag{3}$$

where x, y, z are cartesian coordinates, u, v, w are translation degrees of freedom, and $\theta_x, \theta_y, \theta_z$ are rotation degrees of freedom.

If equations (1) to (3) are written in matrix form for all nodes, it would represent a matrix that maps the displacement field between the two configurations and the transformation matrix $\mathbf{T_{coh}}$ is given by,

$$\mathbf{U_{quad}} = \mathbf{T_{coh}}\ \mathbf{U_{rot}} \tag{4}$$

where $\mathbf{U_{rot}}$ is the displacement vector defined in terms of translations and rotations (Configuration 1) and $\mathbf{U_{quad}}$ is the displacement vector defined only in terms of

translations (Configuration 2). The dimension of $\mathbf{T_{coh}}$ is 48×48. At any given time increment, $\mathbf{U_{quad}}$ and $\mathbf{U_{rot}}$ represents the same displacement field.

To interpolate the displacement in the configuration 2, quadratic shape functions, $\mathbf{N_{quad}}$, of a two-dimensional element is assembled from both the surfaces of a cohesive element. For configuration 1, new shape functions need to be derived from $\mathbf{N_{quad}}$ using $\mathbf{T_{coh}}$ of the cohesive element by,

$$\mathbf{N_{rot}} = \mathbf{N_{quad}}\ \mathbf{T_{coh}} \tag{5}$$

where $\mathbf{N_{rot}}$ is the shape function to interpolate the displacements in configuration 1. The displacement vector, $\boldsymbol{\delta}$, at multiple integration points can be interpolated from $\mathbf{U_{quad}}$ using quadratic shape functions, $\mathbf{N_{quad}}$. The traction vector, $\boldsymbol{\tau}$, is then calculated using a cohesive law. In the current work, a bi-linear traction separation law [5] developed at the University of Bristol is used to model the crack initiation and propagation defined by an energy criterion.

3.2. Higher Order AMS

Insertion of cohesive elements in a finite element mesh before the start of an analysis requires significant effort and introduces a finite stiffness between the continnum elements. This can alter the compliance of an undamaged structure [7] and also the manner and speed with which dynamic stress waves propagate through it. With Higher order Adaptive Mesh Segmentation (AMS), the insertion of the proposed cohesive elements is performed 'on-the-fly' *i.e.* the displacement discontinuities in the out-of-plane direction are modelled by introducing cohesive behaviour between the continuum elements according to a physically based criterion and without user intervention. The Higher order AMS is implemented as a user element in the commercial finite element software LS-DYNA. The new element formulation contains both the

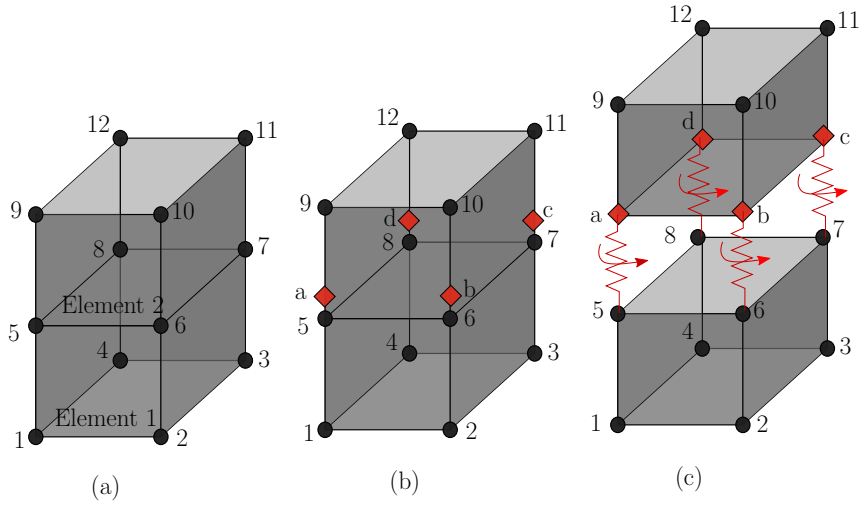

Figure 3: Element segmentation operation, (a) Global numbering of nodes before segmentation at $t < t_s$; (b) At the time of segmentation, new nodes are initiated from the location of existing nodes by mapping field and state variables at $t = t_s$; (c) Cohesive elements with rotations are initiated after segmentation at $t > t_s$.

continuum element formulation and the cohesive element formulation described in Section 3.1.

A compatible continuum element formulation [26], 8 node hexahedral elements with nodal rotations (48 DOF), is used as the continuum element in Higher order AMS. To define the mass matrix for the additional degrees of freedom, rotational inertia is used. A multiplicative factor (α) is used with the rotational inertia to obtain a stable time step while not affecting the global behaviour of the numerical model. This continuum element [26] is also available as a built-in library element in LS-DYNA as ELFORM = 3.

Different stages of segmentation are shown schematically in Figure 3. An element is selected for segmentation upon reaching a segmentation initiation criterion based on the stress tensor at time t_s. New nodes (a,b,c,d), shown in Figure 3b, are initiated

from the location of existing nodes. Existing element connectivity in LS-DYNA cannot be updated. Hence, the element connectivity is updated with the new nodes and time integration of these new nodes is performed at the end of every increment within the user subroutine. State variables of the new nodes, available only within the user subroutine, can be visualised by writing additional output files. Cohesive segments are initiated based on the updated connectivity as shown in Figure 3c; the red coloured nodes and the cohesive segments belong internally within the user subroutine. Also, these cohesive segments are initiated a traction vector, compatible with the surrounding stress field to prevent the introduction of numerical errors.

Standard elements from LS-DYNA (ELFORM = 3) are used in the regions of mesh where delamination is not expected to initiate and also the computational times of built-in library elements are faster. Hence, Higher order AMS can be used along with this LS-DYNA library element in delamination modelling.

3.3. Impactor modelling

A soft body (or gelatine) displays fluid-like behaviour when impacting a stiffer target material, such as carbon-fibre reinforced polymer material. Therefore, to model the soft body impact and its hydrodynamic response, Smooth Particle Hydrodynamics (SPH) is used. SPH also avoids instabilities associated with Lagrangian meshes undergoing severe element distortion.

The pressure-volume behaviour is described through equation of state (EOS). The EOS parameters are derived from Hugoniot impact tests for 20 % gelatine by weight [27]. The shock velocity, U_s, is related to the particle velocity, U_p, by

$$U_s = 1.57 + 1.77\ U_p. \tag{6}$$

This is implemented in LS-DYNA via keyword *EOS_LINEAR_POLYNOMINAL with corresponding constants ($c_0 = 0; c_1 = 2613; c_2 = 6637; c_3 = 8671$). Material

card *MAT_NULL is also used to model the volumetric behaviour of the impactor with a negative cut-off pressure.

3.4. Continuum modelling

The material properties used for numerical analysis of the SBBB test are shown in Table 1. The key elastic modulus for the test coupon behaviour is the fibre direction modulus, E_{11}, since the layup is unidirectional and the main deformation mode is bending. For carbon-fibre, fibre direction properties are generally not considered to be rate dependent [28, 29]. The transverse matrix dominated modulus E_{22}, that might be expected to be more rate dependent, does not affect the bending deformation here. This assumption to neglect strain rate dependency does not cause a significant influence in the model formations and this is explained in Section 4.1.

In the cohesive law, fracture energy is the governing parameter for modelling delamination progression in the case of a pre-crack, as is used here. Rate dependence of the initiation stresses can thus be ignored. For IM7/8552, strain rate dependent 3-ENF Mode II tests revealed that the fracture energy is 0.97 N/mm [30] for high strain rate cases and 0.2 N/mm for Mode I fracture energy in high strain rate tests using DCB specimens [31]. Similar values are used in the current work.

The composite layup is homogenised with twelve elements of size 0.5 mm in the through-thickness direction. The mesh size used for the in-plane direction of the specimen is 1 mm; this mesh size was chosen based on quasi-static tests from [18] and a detailed analysis on mesh sizes in shown in Section 4.3. Similar to the experiments a pre-crack of length 20 mm is modelled by using cohesive elements of negligible interface strength and fracture energy. The penalty stiffness helps to avoid the interpenetration of elements. The model setup is shown in Figure 7a. Matrix cracks are assumed to have negligible influence on the impact-driven delamination crack

Table 1: Material parameters for IM7/8552 used in benchmark cases

E_{11} (GPa)	$E_{22} = E_{33}$ (GPa)	$G_{12} = G_{13}$ (GPa)	G_{23} (GPa)	$\nu_{12} = \nu_{13}$	ν_{23}
161	11.38	5.17	3.98	0.32	0.43
G_{Ic}(N/mm)	G_{IIc}(N/mm)	$\sigma_{\mathrm{I,max}}$(MPa)	$\sigma_{\mathrm{II,max}}$(MPa)	K_{I} (N/mm^3)	K_{II} (N/mm^3)
0.2	1.0	60.0	90.0	10^4	10^4

propagation and so are ignored in the current numerical model.

4. Results and Discussion

4.1. SBBB Model Validation

The numerical model is initially validated for displacement time history via high speed video from experiments, in order to test the ability of the model to represent physical specimen behaviour. Higher order AMS is assigned to the row of elements located near the pre-crack region and therefore where delamination is expected to initiate (green zone in the model in Figure 7). The rest of the laminate is modelled with elements of compatible degrees of freedom, 8-node hexahedral elements with nodal rotations, available as (ELFORM - 3) in LS-DYNA (red zone in the model in Figure 7).

Linear and quadratic bulk viscosity values of 0.06 and 1.5 were used in numerical models. Finally, analysis was conducted over 2.5 ms.

Figure 4 shows the displacement *vs.* time curve at the specimen centre-line for the experiment and Higher order AMS for the impact velocity of 88 m/s. It can be observed that the displacement history of Higher order AMS at the point of impact compares well with experimental results. The numerical model using higher

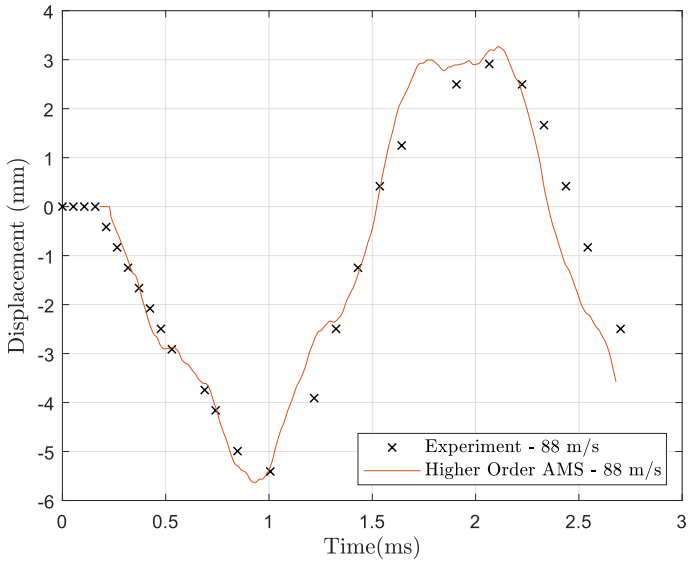

Figure 4: Comparison of centre-line displacement-time history obtained for a projectile with an initial velocity of 88 m/s.

order AMS captures the maximum displacement in both the positive and negative curvature of bending. Also, the assumption to neglect strain rate dependency does not cause a significant influence in model deformations. Impact loading creates a change in curvature locally in the proximity of the impact zone, before the entire specimen is subjected to bending.

4.2. Threshold Velocity

The proposed cohesive element formulation is used to perform threshold velocity calculations in this section. Minor changes in the location of impact can cause considerable change in the delamination growth for a given impact velocity. As such, it is critical to understand the actual location of impact from experiments. In this context, the results are presented in two different sections: (i) a section where the

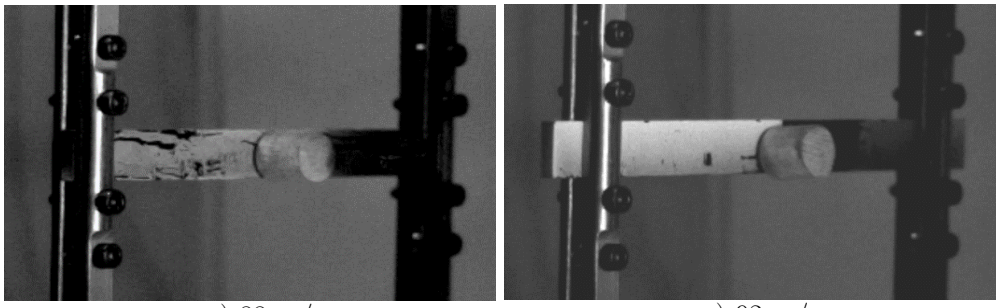

a) 88 m/s a) 92 m/s

Figure 5: Experimental setup in SBBB test showing the offset of projectile in the impact plane under different impact velocities.

centroid of impactor is assumed to coincide with the centroid of the plane of impact (ii) a section where the actual location of impact from experiments are considered.

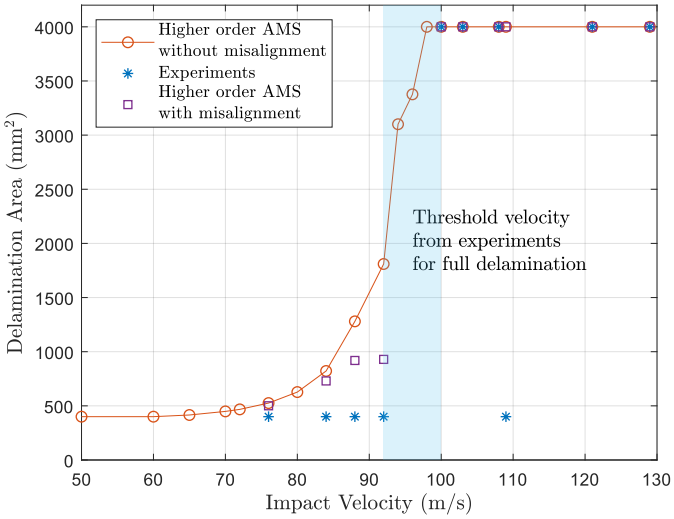

Figure 6: Delamination area obtained for different impact velocities. A mesh size of 1 mm was used for all models.

Table 2: Misalignment details of the projectile at various impact velocities

Impact velocity (m/s)	76	84	88	92	100	103	108	121
offset in the x-direction (mm)	4.2	3.2	1.2	1.3	0.7	0.9	5.8	2.9
offset in the y-direction (mm)	0.0	5.0	0.9	3.3	0.0	0.4	1.7	0.0

4.2.1. Without Eccentricity

The threshold velocity is calculated numerically by varying the impact velocity at an interval of 4 m/s and is plotted in Figure 6. A cohesive element is considered to have failed when all the integration points have reached a damage variable equal to 1 (0 - no failure; 1- full failure). At this point, traction is not generated across the cracked surfaces and they can slide past each other. However, the interpenetration is avoided due to the presence of a penalty stiffness.

From the experiments, it was found that specimens reached full delamination when the impact velocity was more than 100 m/s. Similar behaviour has also been found using higher order AMS. When subjected to 98 m/s, the delamination has traversed along the entire length of the specimen from the pre-defined crack.

Also, a stable crack growth is obtained when subjected to velocities slightly lower than the threshold velocity. The delamination growth at different time increments when subjected to an impact velocity of 88 m/s, is shown in Figure 7. The cross-sectional view (x-z plane) of the numerical model is shown along with the damage plot in the plane of impact (mid-plane through the thickness). The damage growth increases with the time and maximum damage is attained at 0.3 ms.

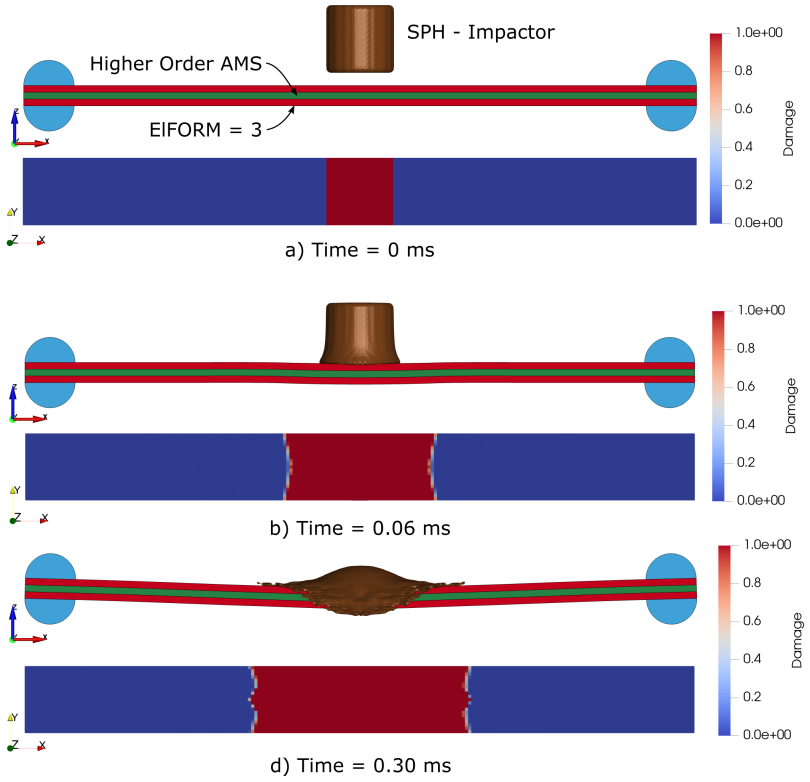

Figure 7: Damage progression in SBBB test specimen subjected to an initial velocity of 88 m/s. The damage growth has stopped at 0.3 ms. (Mesh size 1 mm.)

4.2.2. With Eccentricity

In the experiments, an offset of the projectile in the plane of impact (x-y plane) can occur, as shown in Figure 5, and it results in a change in the contact area (offset in x-direction) as well as the loss of symmetry (offset in y-direction). This can cause a change in the local stress state and the delamination propagation. A careful investigation of high speed camera images revealed the magnitude of offsets and they are listed in Table 2.

The threshold velocity calculations were repeated for the updated impact locations and the results are plotted in Figure 6. The threshold velocity remains similar when

Table 3: Calculation of delamination area using different mesh sizes with linear elements and Higher order AMS at an impact velocity of 88 m/s. The values obtained with Higher order AMS are shown in bold and within parentheses.

Mesh size in-plane(x)			0.5 mm	1.0 mm	1.5 mm	2 mm
Number of Elements			400	200	133	100
Through	1.0 mm	6	1480	1202 (**1450**)	702 (**1346**)	435 (**984**)
thickness	0.75 mm	8	1460	1119 (**1330**)	580 (**1380**)	439 (**905**)
direction	0.6 mm	10	1460	939 (**1319**)	522 (**1382**)	441 (**1038**)
(z)	0.5 mm	12	1340	1090 (**1290**)	489 (**1385**)	447 (**1060**)

compared to numerical models without offset, but there is a significant reduction in the delamination area for impact velocities slightly lower than the threshold velocity. Also, it can be seen that an offset in the y-direction cause a considerable change in the area of delamination when compared to the offset in x-direction. It is primarily due to the change in the contact area of the projectile.

The assumption to perform numerical modelling in the absence of matrix cracks did not appear to have a quantitative influence on the results. The presence of a pre-existing crack, located between two zero degree plies, in this test method initiates delamination, based on the impact velocity, and the energy is dissipated by the delamination growth.

4.3. Comparison with Linear Elements

To compare the computational benefits obtained with Higher order AMS over linear elements, the SBBB test with an impact velocity of 88 m/s is chosen; linear elements available in LS-DYNA are used for the comparison. The numerical models are anal-

Table 4: Number of degrees of freedom (DOF) required to achieve convergence in the delamination area.

	Mesh size			No. of	No. of	Reduction in
	x	y	z	elements	DOF	computational cost
Linear elements	0.5	0.5	1.0	96000	288000	-
Higher order AMS	1.5	1.5	1.0	10374	62444	65 %

ysed with varying number of elements or mesh size in the in-plane (x and y) and the through thickness direction (z), as shown in Table 3, and their delamination areas are calculated; Higher order AMS values are shown within parentheses.

To understand the rate of convergence obtained with both set of numerical models, a third numerical model with a highly refined mesh of 0.25 mm in the x and y-direction and 0.5 mm in the z-direction is generated using linear elements. This model is taken as the benchmark to study the rate of convergence with the delamination area obtained being 1340 mm^2; the rate of convergence is higher, if an element formulation approaches this value with fewer degrees of freedom. The curvature change around the impact location requires higher number of degrees of freedom to calculate displacements and tractions than quasi-static benchmark cases.

It can be observed from Table 3 that the Higher order AMS approached the benchmark value with an in-plane mesh size of 1.5 mm. By contrast the coarsest in plane mesh with linear elements that approached the benchmark value was 0.5mm. Also, consistent results are obtained for different AMS mesh sizes in the z-direction. Based on the data in Table 4, one can see that Higher order AMS requires 4.6 times fewer number of degrees of freedom than linear elements.

To perform the comparison in computational cost, linear elements were also implemented as user defined elements. The two modelling methods, implemented as user defined elements and shown in Table 4, were analysed using a high performance cluster node with 16 CPUs and a 65 % reduction in computational cost was obtained by using Higher order AMS over linear elements.

5. Conclusions

A novel cohesive element formulation for delamination in a composite specimen has been applied to the case of dynamic loading due to impact. By using this element, fine mesh requirement associated with linear cohesive elements can be alleviated, retaining the essential crack tip driving mechanisms and thus not compromising model accuracy. The presence of additional degrees of freedom gives a C^1 continuity in the cohesive element and helps to solve problems with considerably fewer degrees of freedom. Additionally, Adaptive Mesh Segmentation (AMS) is included to introduce cohesive elements 'on-the fly', which eliminates the pre-processing steps required to introduce those elements.

The element formulation was validated against experimental results from SBBB tests, which allowed for replication of the stress state inside a specimen without the spurious stress induced by boundary conditions. Threshold velocity calculations from numerical models agreed well with the experimental data. Damage growth was also investigated for the eccentricities observed in the experiments in regard to impact location. It was observed that , in both experiment and models, while eccentricities resulted in a change in the damage growth below the threshold energy level, the effect of eccentricity is minimal after crossing the threshold energy.

This method could be extended in the future to model in-plane failure behaviour of composite specimens via incorporating continuum damage mechanics methods. Such

an integrated method, along with the improvements in computational efficiency pave the way for a general capability to accurately model failure of large scale composite structures with the correct driving mechanisms and coarser meshes thus improving the capability for virtual testing of composites.

Acknowledgements

This work was supported by the Engineering and Physical Sciences Research Council (EPSRC) through the Centre for Doctoral Training in Advanced Composites at the University of Bristol (Grant no. EP/L016028/1). The authors would also like to acknowledge Rolls-Royce plc for their support of this research through the Composites University Technology Centre (UTC) at the University of Bristol.

References

[1] J. P. Hou, N. Petrinic, C. Ruiz, A delamination criterion for laminated composites under low-velocity impact, Composites Science and Technology 61 (14) (2001) 2069–2074. doi:10.1016/S0266-3538(01)00128-2.

[2] S. Guinard, O. Allix, D. Guédra-Degeorges, A. Vinet, A 3D damage analysis of low-velocity impacts on laminated composites, Composites Science and Technology 62 (4) (2002) 585–589. doi:10.1016/S0266-3538(01)00153-1.

[3] M. R. Wisnom, The role of delamination in failure of fibre-reinforced composites, Philosophical Transactions of the Royal Society A: Mathematical, Physical and Engineering Sciences 370 (1965) (2012) 1850–1870. doi:10.1098/rsta.2011.0441.

[4] O. Allix, P. Ladevèze, Interlaminar interface modelling for the prediction of

delamination, Composite Structures 22 (4) (1992) 235–242. doi:10.1016/0263-8223(92)90060-P.

[5] W. G. Jiang, S. R. Hallett, B. G. Green, M. R. Wisnom, A concise interface constitutive law for analysis of delamination and splitting in composite materials and its application to scaled notched tensile specimens, International Journal for Numerical Methods in Engineering 69 (9) (2007) 1982–1995. doi:10.1002/nme.1842.

[6] A. Turon, C. G. Dávila, P. P. Camanho, J. Costa, An engineering solution for mesh size effects in the simulation of delamination using cohesive zone models, Engineering Fracture Mechanics 74 (10) (2007) 1665–1682. doi:10.1016/j.engfracmech.2006.08.025.

[7] R. de Borst, J. J. Remmers, A. Needleman, Mesh-independent discrete numerical representations of cohesive-zone models (jan 2006). doi:10.1016/j.engfracmech.2005.05.007.

[8] P. W. Harper, S. R. Hallett, Cohesive zone length in numerical simulations of composite delamination, Engineering Fracture Mechanics 75 (16) (2008) 4774–4792. doi:10.1016/j.engfracmech.2008.06.004.

[9] R. Krueger, Virtual crack closure technique: History, approach, and applications, Applied Mechanics Reviews 57 (2) (2004) 109–143. doi:10.1115/1.1595677.

[10] A. Tabiei, W. Zhang, Composite Laminate Delamination Simulation and Experiment: A Review of Recent Development, Applied Mechanics Reviews 70 (3), 030801 (06 2018). doi:10.1115/1.4040448.

[11] E. Pietropaoli, A. Riccio, On the robustness of finite element procedures based on virtual crack closure technique and fail release approach for delamination growth phenomena. definition and assessment of a novel methodology, Composites Science and Technology 70 (8) (2010) 1288 – 1300. doi:10.1016/j.compscitech.2010.04.006.

[12] N. Moës, T. Belytschko, Extended finite element method for cohesive crack growth, Engineering Fracture Mechanics 69 (7) (2002) 813–833. doi:10.1016/S0013-7944(01)00128-X.

[13] J. M. Melenk, I. Babuška, The partition of unity finite element method: Basic theory and applications, Computer Methods in Applied Mechanics and Engineering 139 (1-4) (1996) 289–314. doi:10.1016/S0045-7825(96)01087-0.

[14] A. Hansbo, P. Hansbo, A finite element method for the simulation of strong and weak discontinuities in solid mechanics, Computer Methods in Applied Mechanics and Engineering 193 (33-35) (2004) 3523–3540. doi:10.1016/j.cma.2003.12.041.

[15] B. Y. Chen, S. T. Pinho, N. V. De Carvalho, P. M. Baiz, T. E. Tay, A floating node method for the modelling of discontinuities in composites, Engineering Fracture Mechanics 127 (2014) 104–134. doi:10.1016/j.engfracmech.2014.05.018.

[16] L. F. Kawashita, A. Bedos, S. R. Hallett, Modelling Mesh Independent Transverse Cracks in Laminated Composites with a Simplified Cohesive Segment Method, Tech. Rep. 2 (2012).

[17] T. Belytschko, W. Liu, B. Moran, Nonlinear Finite Elements for Continua and Structures, John Wiley & Sons, Ltd, 2000.

[18] J. Selvaraj, S. Mukhopadhyay, L. F. Kawashita, S. R. Hallett, Modelling delaminations using adaptive cohesive segments with rotations in dynamic explicit analysis, Engineering Fracture Mechanics 245 (2021) 107571. doi:https://doi.org/10.1016/j.engfracmech.2021.107571.

[19] J. Selvaraj, L. Kawashita, G. Allegri, S. Hallett, Adaptive Mesh Segmentation for Modelling Dynamic Delamination Initiation and Propagation in Thick Composite Laminates, in: 12th European LS-DYNA conference, 2019.

[20] T. Menouillard, T. Belytschko, Smoothed nodal forces for improved dynamic crack propagation modeling in XFEM, International Journal for Numerical Methods in Engineering 84 (1) (2010) 47–72. doi:10.1002/nme.2882.

[21] S. R. Hallett, Three-point beam impact tests on T300/914 carbon-fibre composites, Composites Science and Technology 60 (1) (2000) 115–124. doi:10.1016/S0266-3538(99)00099-8.

[22] L. Greve, A. K. Pickett, Delamination testing and modelling for composite crash simulation, Composites Science and Technology 66 (6) (2006) 816–826. doi:10.1016/j.compscitech.2004.12.042.

[23] S Read, inventor; Rolls-Royce PLC, assignee, Test apparatus and method of testing. US 7,845.207 B2 (Dec. 2010).

[24] G. Mohamed, G. Kalwak, S. R. Hallett, M. Jevons, Modelling soft body impact of through-thickness reinforced composites, in: 16th European Conference on Composite Materials, Seville, Spain, 2014.

[25] Y. M. Le Cahain, J. Noden, S. R. Hallett, Effect of insert material on artifi-

cial delamination performance in composite laminates, Journal of Composite Materials 49 (21) (2015) 2589–2597. doi:10.1177/0021998314550428.

[26] S. M. Yunus, T. P. Pawlak, R. D. Cook, Solid elements with rotational degrees of freedom: Part 1—hexahedron elements, International Journal for Numerical Methods in Engineering 31 (3) (1991) 573–592. doi:10.1002/nme.1620310310.

[27] C. J. Shepherd, G. J. Appleby-Thomas, P. J. Hazell, D. F. Allsop, The dynamic behaviour of ballistic gelatin, in: AIP Conference Proceedings, Vol. 1195, 2009, pp. 1399–1402. doi:10.1063/1.3295071.

[28] Y. Zhou, Y. Wang, Y. Xia, S. Jeelani, Tensile behavior of carbon fiber bundles at different strain rates, Materials Letters 64 (3) (2010) 246 – 248. doi:https://doi.org/10.1016/j.matlet.2009.10.045.

[29] N. Taniguchi, T. Nishiwaki, H. Kawada, Tensile strength of unidirectional cfrp laminate under high strain rate, Advanced Composite Materials 16 (2) (2007) 167–180. doi:10.1163/156855107780918937.

[30] M. Yasaee, G. Mohamed, A. Pellegrino, N. Petrinic, S. R. Hallett, Strain rate dependence of mode ii delamination resistance in through thickness reinforced laminated composites, International Journal of Impact Engineering 107 (2017) 1 – 11. doi:https://doi.org/10.1016/j.ijimpeng.2017.05.003.

[31] H. Cui, Y. Mahadik, S. R. Hallett, I. K. Partridge, G. Allegri, S. A. Ponnusami, N. Petrinic, Coupon scale z-pinned im7/8552 delamination tests under dynamic loading, Composites Part A: Applied Science and Manufacturing 125 (2019) 105565. doi:https://doi.org/10.1016/j.compositesa.2019.105565.